COMPUTATIONAL FLUID DYNAMICS AND EXPERIMENTAL INVESTIGATION OF AIRPLANE STALL DYNAMICS WITH WING CONTAMINATION

M.E. Beyers*, M. Mamou*, A.P. Brown, Y. Mébarki***
***Aerodynamics Laboratory, Building U66, **Flight Research Laboratory, Building U61**
Institute for Aerospace Research, National Research Council, Ottawa, ON, K1A 0R6

Keywords: *dynamic stall, roughness, CFD, flight testing, infrared thermography*

Abstract

A research program is under way to investigate factors influencing transport airplane stall onset at take off. Methodologies have been developed to study unsteady aerodynamics of airplane dynamic stall for both straight- and swept-wing airplane types. The conditions associated with the take off maneuver with wing contamination are replicated in flight tests at altitude and complemented by ground runs. A roughness model is introduced to simulate arbitrary wing contamination. An unsteady Navier-Stokes analysis using two modified turbulence models will simulate the combined effects of roughness, pitch rate and ground proximity. Prediction of the unsteady flow separation on airplane wings in ground effect will be accomplished by analytically linking the flight test results and CFD simulations. CFD results are presented for a steady state rough-airfoil case and for a clean oscillating airfoil in and out of stall. The analytical approach is outlined and results are presented, including flight test data from the first phase, details of roughness simulation, instrumentation diagnostics and CFD validations.

1 Introduction

Throughout the history of jet air transportation, there have been periodic occurrences of dynamic stall on take off or go-around, often followed by wing drop [1]. The phenomenon has been associated with appreciable pitch rates, and quite often, wing surface contamination [1]-[2]. The Institute of Aerospace Research (IAR) of the National Research Council (NRC) has embarked upon a research project to examine the phenomenon. Flow physics considerations indicate that the effects of airplane pitch rate, surface roughness and ground proximity are nonlinearly coupled [3]. Concluding that assessments based on superposition of their individual effects would likely lead to misleading predictions, an approach was adopted that simulates the actual stall event in ground effect, in the presence of both pitch rate and surface roughness. A combination of flight tests, computational fluid dynamics (CFD) and engineering analysis was undertaken. Flight tests on the NRC CT-133 straight wing aircraft [4] allowed procedures to be developed during ground tests for take off with wing leading edge roughness, followed by stalling maneuvers at altitude. The extension to swept-wing airplane types is being accomplished with parallel tests on the NRC Falcon DA20. The project is broad in scope and of a multi-disciplinary nature. The purpose of this paper is to outline the approach and new methodologies introduced to address the problem. Some preliminary results from the first two flight test series, details of flow diagnostics, and CFD development and validation are presented.

2 Rationale

For obvious reasons, the actual flight tests involving stalling and/or loss of control cannot be performed near the ground. Hence, a method had to be devised to extrapolate the free-air stalling characteristics to ground proximity. This would use a computational approach wherein the free-air and ground effect unsteady aerodynamics are bridged by flow physics modeling. Both the flight test and CFD simulations would have to account for the effects of wing surface roughness, ground proximity and pitch rate effects. Whereas the unsteady Reynolds averaged Navier-Stokes (URANS) model would be idealized to the case of pure pitching and account for viscous effects and compressibility within the limitations of state of the art turbulence modeling, the flight tests would be designed to elucidate the complete phenomenon of incipient dynamic stall of a transport airplane, which is characterized by viscous coupling of flow separation with airplane pitching and rolling motions. The simulation of wing surface roughness due to in-flight icing and anti-/de-icing fluid contamination would require a roughness model that determines the equivalent sand-grain roughness from practical roughness distributions and coverage. With the premise based on CFD/flight-test integration, considerable emphasis would be placed on instrumentation that could reveal the surface flow separation characteristics during dynamic stalling.

3 Aerodynamic Model

3.1 Flow Physics

The first step was to identify the physical mechanisms underlying the dynamic stall phenomenon. The dominant unsteady flow separation mechanisms for airfoil pitch-up have been identified as accelerated flow and viscous fluid/motion coupling effects [5]. Thus, the onset of flow separation is governed by a combination of pressure gradient lag effects inside and outside the boundary layer [5], and a viscous fluid/motion coupling effect, which has been referred to as the moving wall effect [6]-[7]. During the pitch-up maneuver the boundary layer on the upper surface of the wing is energized through a wall jet-like effect acting close to the stagnation point, where the velocity gradients are very high (Fig. 1).

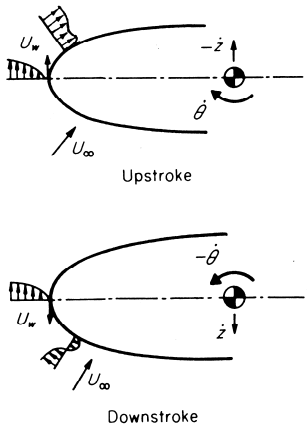

Figure 1: Moving wall effect on an airfoil in pitching and/or plunging motion.

The result is that the boundary layer becomes more resistant to separation, allowing the static stall angle to be exceeded by an increment $\Delta\alpha_s$, the well-known dynamic stall overshoot [8]. On the lower surface, the corresponding adverse effect weakens the boundary layer. The dynamic overshoot of the static stall angle in fully turbulent flow is then:

$$\Delta\alpha_s = \Delta\alpha_{s1} + \Delta\alpha_{s2} \qquad (1)$$

where $\Delta\alpha_{s1} = K_1 \frac{c\dot{\alpha}}{U_\infty}$ and $\Delta\alpha_{s2} = K_2 \frac{\dot{z}_{LE}}{U_\infty}$ are the contributions due to accelerated flow and moving wall effects respectively, and K_1 and K_2 are constants defined in Ref. [5]. The nature of the phenomenon depends on the boundary layer steady state condition. At high angle of attack the peak upper surface flow velocity is developed near the leading edge, and boundary layer transition occurs near the airfoil nose. When the moving wall effect acts on transition before flow

separation, a leading edge separation could be precipitated. Generally, in such a state, airfoils are sensitive to surface condition and freestream turbulence, and the coupling due to any rigid body motion would be a function of the surface roughness. The presence of roughness will alter or eliminate the viscous coupling. As the stall progression on the aircraft wing is fundamentally asymmetric, the lift distribution on a pitching clean wing can be non-uniform when flow separation is present, generating an un-commanded rolling moment. For the plunging wing section, the effect of the boundary layer coupling is dynamically destabilizing, resulting in dynamic mode bifurcations such as wing drop.

The take off maneuver for a transport airplane is characterized by relatively low dimensionless pitch rates $\dot{\alpha}c/2U_\infty$. This results in initially quasi-steady aero-dynamics [5], which is dominated by viscous effects due to the translational motion of the leading edge during pitching or plunging/heaving. Accordingly, a stall onset parameter defined by

$$\Delta\overline{\alpha}_s = \frac{\Delta\alpha_s}{\alpha_s - \alpha_0} \qquad (2)$$

was introduced to link the static and dynamic parameters, where $\Delta\alpha_s$, α_s and α_0 are the dynamic stall overshoot onset angle increment, static stall angle, and zero-lift angle, respectively. The similarity parameter (Eq. 2) is a function of the kinematic, flow, and surface roughness parameters. This simple form was also generalized to static data [3], correlating $\Delta\alpha_{CLmax}/(\alpha_{CLmax} - \alpha_0)$ with the relative roughness height, k/c. Favorable correlation of dynamic stall onset delay was obtained on low Reynolds number (Re) airfoils and on the NRC Harvard airplane at flight Reynolds numbers [3]. This demonstrated a degree of universality of pitch rate effects on dynamic stall onset for the smooth, straight wing case, which was not unexpected in this confined part of the parameter space, considering the dominance of the moving wall effect. Different behavior is expected due to other factors influencing the stall onset parameter, including the roughness effect, promoting (static) stall onset ($\Delta\overline{\alpha}_s < 0$), and Mach number and ground effect, introducing nonlinearities due to changes in stall type or progression. Combined pitch rate, roughness and ground effects could either delay or promote stall. Viewed from another perspective, the susceptibility to small scale roughness may be higher in the presence of coupling with pitch rate and ground effects.

3.2 Analytical Approach

As the flow physics of airplane unsteady stalling is dominated by viscous flow effects [9], not all the parameters leading to loss of control can be simulated simultaneously in flight tests, particularly for conditions near the ground; neither can all the flow mechanisms governing the stall event be simulated by a URANS model. An empirical database is generated comprising unsteady data from both free-air stalling and ground roll tests. To bridge the gap between the free-air and in-ground effect behavior, it is necessary to construct an unsteady aerodynamics model that captures the flow physics governing unsteady stall onset, including how this is affected by pitch rate, surface roughness and ground effect.

Conceptually, it is possible to model the viscous motion coupling in the CFD simulations, but this may not always be practicable or economical. In particular, the viscous-dominated stall onset delay for clean wings cannot easily be predicted at present [9]. However, for the fully-rough wing case, for which CFD can be validated and matched to flight test, the accelerated flow effect on the external flow, circulation lag and boundary layer lag could be captured. Below a certain roughness threshold, the competing flow mechanisms will be determined by boundary layer and roughness characteristics. Then, where the moving wall effect is dominant, the absence

of the dynamic coupling in the URANS model is accounted for in a "dynamically equivalent" simulation, by defining effective kinematic and flow parameters (Fig. 2). Assuming further that there is no bifurcation of the stall type, the behavior is quasi-steady, and the contributions to $\Delta\alpha_s$ can be superimposed (Eq. 1). In the ideal case, a time-accurate Navier-Stokes solution would be desired that models both the roughness and the moving wall effects at high Reynolds numbers; however, the additional turbulence modeling required would be beyond the scope of this investigation.

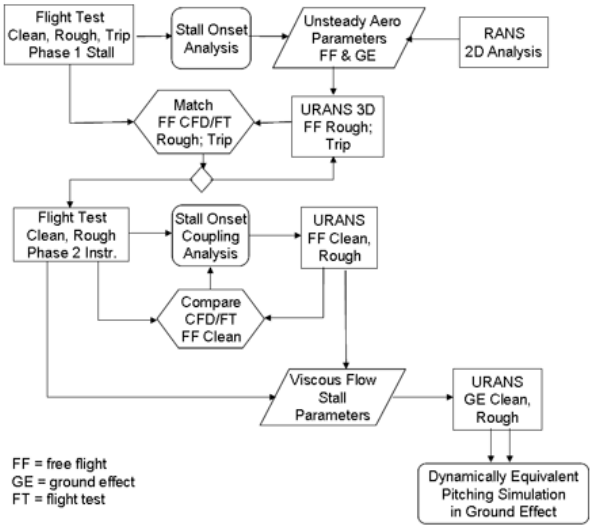

Figure 2: Flow chart of flight test/CFD analysis.

The dynamic coupling effects are extracted through a "stall onset analysis" (Fig. 2) of a series of free-air stalling tests and matched URANS computations, for both clean and rough leading edges. As Fig. 2 shows, the experimental and CFD techniques are fully integrated through the unsteady aerodynamics model. The pitch-rate induced stall onset data $\Delta\overline{\alpha}_s$ (Eq. 2), from both flight test and CFD, are correlated with $\dot{\alpha}c/2U_\infty$ as part of the process ("stall onset coupling analysis" in Fig. 2) for isolating the various viscous and inviscid contributions to the dynamic stall onset. The analysis is restricted to the quasi-steady domain, which is bounded by critical pitch and roll rate boundaries that exclude time history dependent events, including transient phenomena and pitch/roll rate-induced changes in stall type. To transfer the unsteady characteristics from free-air to ground effect, it is assumed that the viscous moving wall effect is unaffected by ground effect induced changes in stall progression; this is justified within the quasi-steady domain of incipient stall. Some of the steady aerodynamic data needed in this scheme can be obtained from 2D RANS analysis. Then, combining the information extracted from flight test analysis and URANS calculations as shown schematically in Fig. 2, a "dynamically equivalent" prediction of stall in ground effect can be made.

3.3 Extension to Swept Wings

The approach to dynamic stall onset on a swept wing airplane is similar, but additional modeling is required as the accelerated flow and moving wall effects are modified by the three dimensionality of the leading edge flow near the stall angle [9]. To handle the increased complexity, additional steps are required in the analytical procedure as well as in flow visualization and diagnostics. The three dimensional (3D) unsteady flow separation mechanisms are discussed in more detail in Ref. [9].

As the swept-wing flow field of the Falcon is highly three dimensional the analysis is more computationally intensive than for the straight-wing airplane, and there is a greater reliance on experimental determination of stall progression. For this reason, 3D flow visualization involving infrared thermography plays a key role.

4 Roughness Simulation

4.1 Experimental Simulation of Wing Roughness

Modeling of surface roughness is an essential part of the program. The CFD approach to turbulent flow over rough surfaces is to model rather than to mesh the

roughness elements. Sandpaper sheets were routinely applied to provide controlled 3D roughness distributions within a confined k_s/k range, where k_s is the equivalent sand grain roughness height [10] and k is the geometric roughness height. To achieve roughness distributions of arbitrary k_s/k and k/c the application of aluminum tape with suitable roughness impressions was developed. A mechanical method was perfected for series production of dimpled aluminum tape for application on the test airplanes.

As the equivalent sand grain roughness is formulated in the turbulence models used here, a practical means of determining k_s from measured roughness characteristics was needed. To this end a new universal correlation of equivalent sand grain roughness was derived (Section 4.2).

The properties of a typical grit particle and the sand grain distribution have to be determined statistically. To find the solidity λ_S of the distribution, i.e. the area covered by roughness per unit surface area, a novel procedure was introduced to discriminate the roughness particles from the backing paper and glue. This procedure involves the digital photography of a sample of sandpaper illuminated by ultraviolet (UV) light, allowing spectral separation between the particles and the paper. In the images, the grit particles appear darker than the backing paper, which becomes luminescent under UV illumination. An image processing tool has been developed to detect automatically the particles and count the area covered by particles. A standardized procedure has been applied to different sandpaper types.

The image of a sample of 3×3 in^2 to be analyzed is divided into nine regions of 1×1 in^2. Each region has its contrast enhanced to correct for spatial non-uniformity of the light excitation. A unique threshold level is used to separate the grit (dark) from the bright paper (light color) on the entire sample. After grit detection, statistics are performed on the results obtained separately for all nine regions to produce the mean grit distribution and the standard deviation. The result for λ_S is given in percent of area covered per unit surface area for each region (Fig. 3). From the knowledge of the grit distribution in the images, the contours of the grit are produced and superimposed (in white) on the original sandpaper image (Fig. 4). This serves as a verification tool for the user. The detection parameter (sample threshold level) can then be adjusted to improve the quality of the detection, as needed.

4.2 Modeling of 3D Roughness

Recognizing that the effectiveness of an individual roughness element in eddy formation within the boundary layer is as much a function of the distribution of elements as it is of its own geometric characteristics, an effective roughness height parameter k_e/k, which is related to k_s, is determined by considering the mutual interference of individual roughness elements. This leads to effective values of the solidity parameter and drag of each protuberance. Accordingly, an effective 3D distributed roughness resistance parameter Φ_{3DR} was introduced

$$\Phi_{3DR} = fn(\, k/c,\, \lambda_S,\, \lambda_F,\, k_e/c) \qquad (3)$$

where λ_F is the frontal solidity.

When correlating the parameter k_s/k with Φ_{3DR} a linear correlation is obtained. This is illustrated in Fig. 5 for Schlichting's roughness elements [11]. In existing work on the correlations of k_s/k (Ref. [10]) or $k_s/(C_D k)$ (Ref. [12]) with λ_F, two regimes are apparent, where the roughness effect respectively increases and decreases with λ_F. The present result (Eq. 3) is most convenient for the determination of equivalent sand grain roughness k_s/k, as it merges the two regimes and is applicable to arbitrary roughness types.

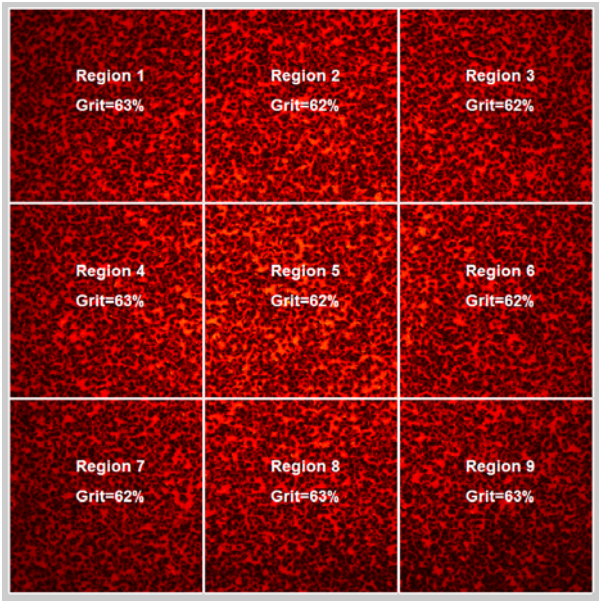

Figure 3: Detection results for sample of #40 grit sand paper displayed on original (raw) image. Mean value is 62.4%, $1\sigma = 0.5\%$ from all regions.

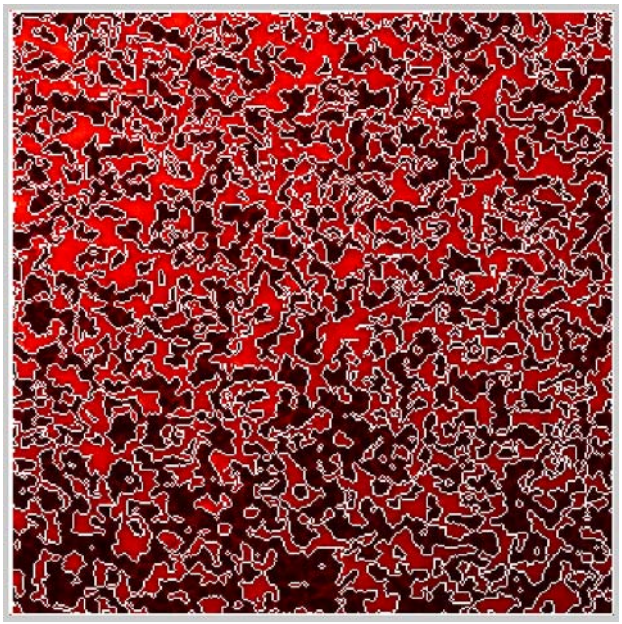

Figure 4: Close-up view of the bottom right corner region (Region #9) with the grit contour superimposed (in white).

5 Instrumentation

On both research airplanes, wing pressure distributions are measured at two spanwise wing stations by means of closely spaced pressure taps, together with a set of pressure transducers. In the case of the Falcon, infrared thermography (IR) provides data on the boundary layer flow (see Section 3.3).

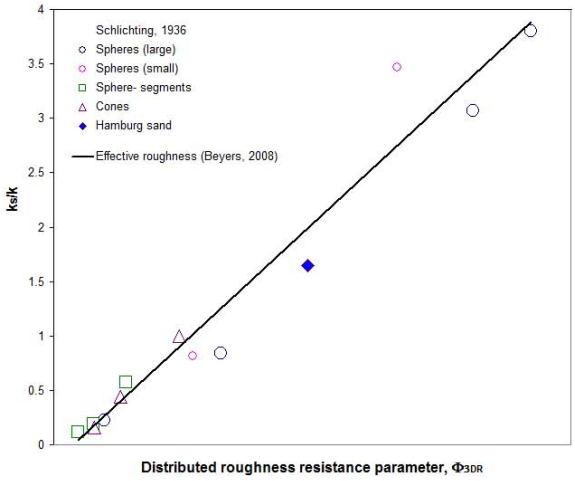

Figure 5: Correlation of k_s/k with the distributed roughness parameter for Schlichting's [11] roughness elements.

A FLIR SC3000 camera is used, which is sensitive in the far infrared and capable of capturing 60 images per second, with an image resolution of 240×320 pixels. The camera is focused on the wing through a dummy emergency exit door, without window in the case of ground tests, or equipped with a special IR window in the case of flight tests. The camera and related equipment (a PC, control box, etc.) are installed on a rack secured inside the aircraft. The wing top surface has been coated with matt black paint to increase the surface emissivity and minimize the level of background reflections. Figure 6 shows a photograph of the Falcon left wing painted black and covered with 2-inch long white tufts for surface flow visualization. Due to the presence of a wing fence, the field of view is restricted to a region of the outboard wing up to the wing tip and to approximately 97% of the wing chord. The wing leading edge and the first one percent of the chord are not visible in the images.

The IR camera start event is controlled by the on-board data acquisition system. During a typical ground test, when the aircraft speed reaches about 90 knots, the IR

camera is triggered and records the data for 25 seconds. Figure 7 shows some of the parameters (speed and pitch angle) acquired during a ground test versus run time.

Figure 6: Photograph of the Falcon aircraft with the left wing painted black and covered with tufts for flow visualization. The IR camera is located behind the emergency exit door.

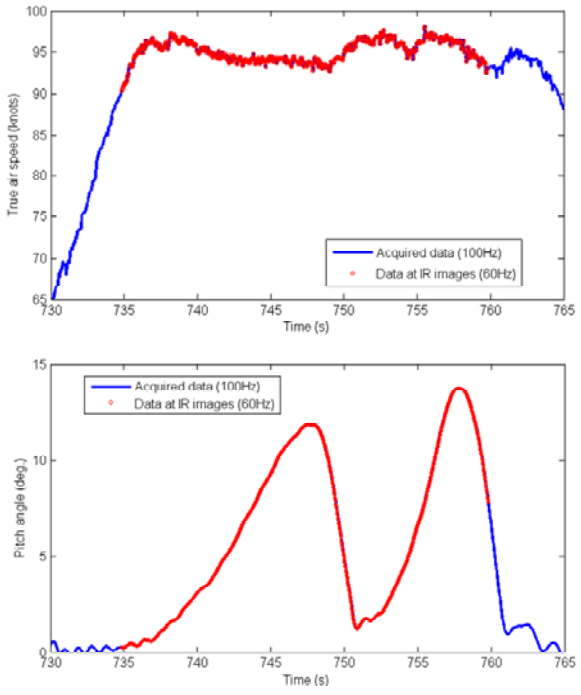

Figure 7: Speed and pitch profiles from the first run of the ground test. Red symbols correspond to IR image acquisition (1500 images).

The principle of infrared thermography for flow visualization is based on the variation of heat transfer coefficients with air flow characteristics. The heat transfer coefficient is greater for an attached flow than for a separated flow. In the present study, the central part of the wing, containing fuel, is warmer than the air (T_{amb} ~ -15°C). Therefore, the attached flow is continuously cooling the wing down. As soon as a flow separation region occurs on the wing (e.g. during the pitch-up maneuver), the wing temperature tends to increase and the temporal temperature variation is an indication of the flow characteristics on the wing. After flow separation, the wing has become locally warmer. The wing will be cooled down again if the flow reattaches on the wing (e.g. during the pitch-down maneuver). In this case, the temperature gradient is reversed. This is illustrated in Fig. 8, showing a raw image (a) and the same image after processing (b).

The raw image temperature distribution (Fig. 8 a) is non-uniform due to wing internal heat sources and various heat capacities (droop, main wing section and flap). Additional artifacts (reflections of the runway lights) were noticed when the aircraft was pitched to high angles of attack on certain runways.

Various data processing methods were evaluated to extract relevant information from the IR images. The most interesting was found to be the computation of the temperature difference or gradient (ΔT) using a sliding reference image. This refers to an analysis whereby the current image is being compared with an image lagging behind it by a fixed number of images (ΔI). This process has the advantage of cancelling out most of the wing deformations under aerodynamic loading (provided that ΔI is not too large).

The computation of a temperature gradient using ΔI=25 images produces a temperature difference with most of the non-uniformities and artifacts removed. In the processed image (Fig. 8 b), the trailing edge separation is visible as well as a leading edge separation close to the wing tip.

This process was applied to the complete run. Some characteristic images extracted from the second pitch-up of the first run are shown in Fig. 9. The first image, at a pitch angle of 4.49°, shows a

uniform temperature gradient, indicating that the flow field remained unchanged between the current and reference images. This is interpreted as attached flow everywhere on the wing. The next two images, from pitch angles 7.49° to 8.75°, display the onset and development of spanwise separation near the trailing edge along the entire visible portion of the span.

The following image, at 10.0°, is particularly interesting, showing the separation front reaching some tufts, clearly no longer aligned with the wing surface. In the next image, at a pitch angle 13.3°, the flow has separated from the wing, as indicated by the disorganized tufts. The last image, recorded during pitch-down at 11.91°, shows the trailing edge flow reattachment as the wing cools down and the temperature decreases (negative gradients).

During the tests, it was realized that the tufts were highly visible in the infrared images. This means that information on the flow separation progression obtained from the temperature gradients could be well correlated with the tufts on the same images, a positive result for the analysis.

6. Dynamic Stall Flight Tests

Dynamic stalling flight tests constitute the central element of the methodology for predicting stall behavior in ground proximity (Section 3). The flight testing techniques have been described in some detail in Refs. [3] and [4]. Two dynamic stalling flight test series have been conducted in free-air at altitude, with complementary ground runs, using the NRC CT-133 research jet. Examples of the results from the first series are presented here.

The instrumentation of the NRC CT-133 has been recently upgraded [3], covering a customized air data sensing system, and the NRC FRL integrated inertial reference and navigation system (FIIRNS). The data acquisition system acquires air and inertial data at 600 Hz, optimized for atmospheric research, although excessive for the present flight dynamic research.

Straight flight stalling maneuvers were conducted in the en-route (gear and flaps retracted) and take off (gear down and flaps deployed at 32°) configurations. The airplane was landed in the take off configuration, generally using an extended flare maneuver at low airborne wheel height above the tarmac, where possible to the point of wing flow separation onset. Each flight consisted of four stalling maneuver sets.

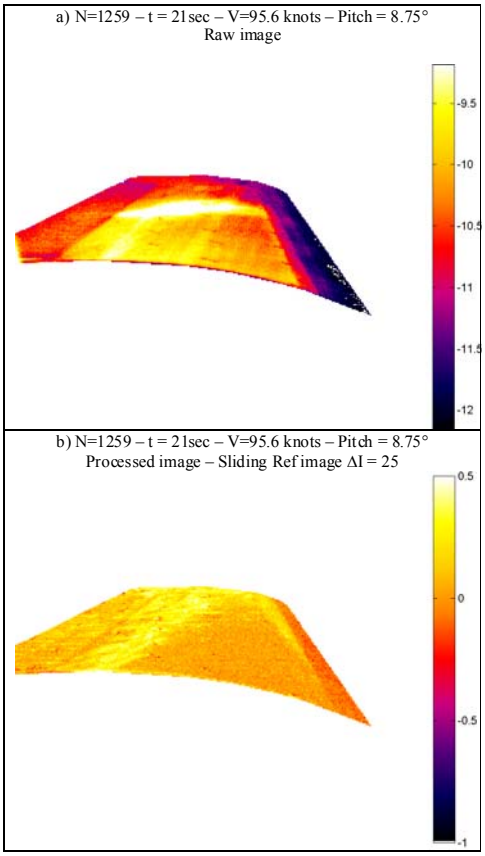

Figure 8: a) Wing surface temperature at t = 21s after first IR image (Run time = 756 s in Fig. 7). b) Wing temperature gradient for the same image processed using a sliding reference.

The reference wing surface roughness configurations consisted of clean (i.e. no additional roughness added), #180, #120, #80 and #40 grades of sandpaper applied from the leading edge to 8% of the chord on the upper and lower surfaces. Alternatively, dimpled aluminum tape produced to appropriate specifications was applied. Stall onset was invariably identified by the onset

of significant angular acceleration; generally as a roll instability with nearly concurrent pitch break instability, although, at times, it was a pitch break instability without any significant roll break, or a roll onset followed by a pitch break.

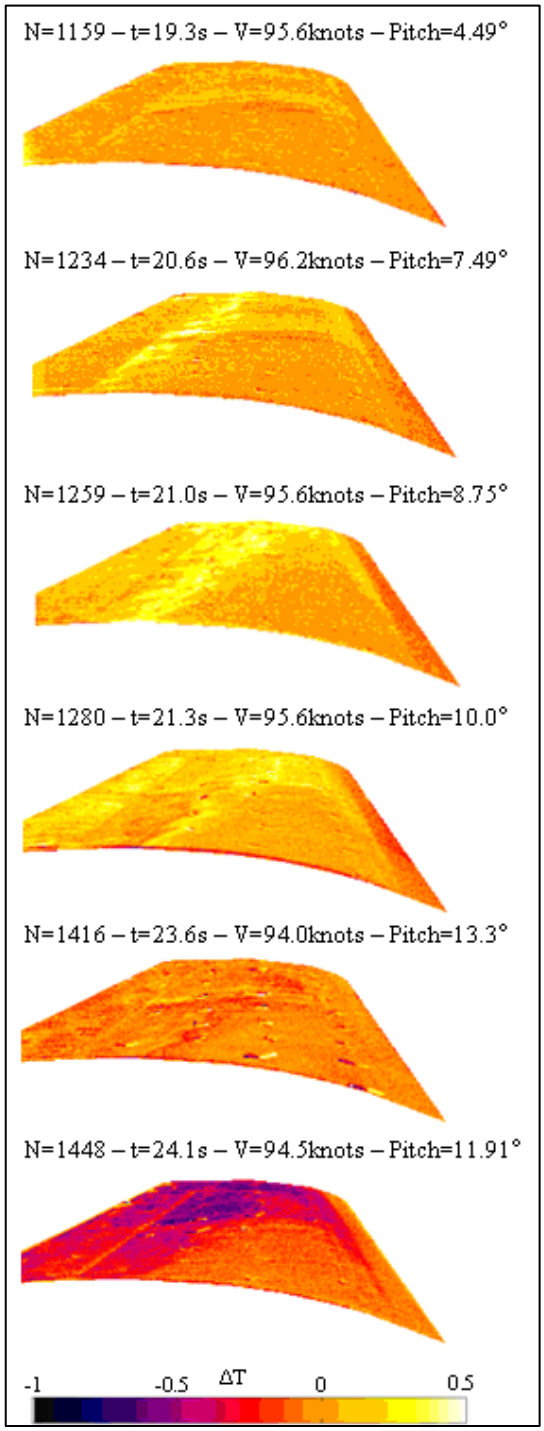

Figure 9: Processed IR images showing temperature gradient. The time given in the images is the time after camera trigger (t=0 s corresponds to run time = 734.8 s).

One result documented has been the bifurcating nature of C_L characteristics with increasing stall entry pitch rate q_{SE} (Figs 10 and 11). Figure 11 illustrates the tendency to roll divergence following pitch up. From the series of tests at different roughness states [4], it was found that the effects of stall entry pitch rate are nonlinearly dependent on the surface roughness.

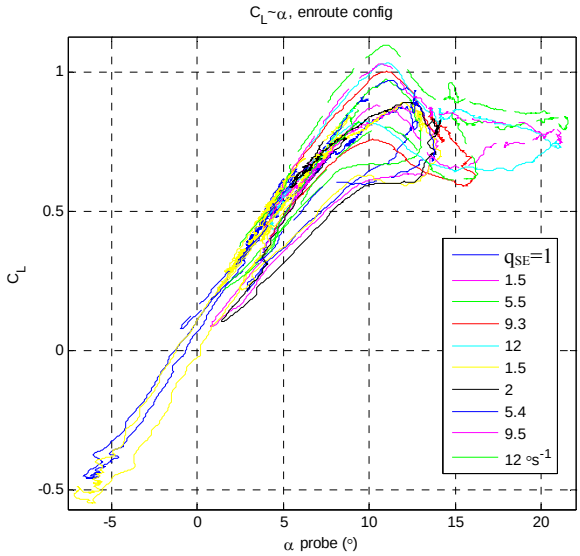

Figure 10: Lift curve segments, showing rounded C_{Lmax} behavior at lower pitch rates (q_{SE} < 5 deg/s), and peaked C_{Lmax} behavior at higher rates (#40 grit sandpaper, en-route configuration, 10 tests).

At lower stall entry pitch rates q_{SE} (q_{SE} < 5 deg/s), the pitch rate increases the stall onset angle α_{SE} and the maximum lift angle α_{CLmax} for the clean wing state, in accordance with previous flight and wind tunnel dynamic stall data ([3] and [8]), whereas in the roughened wing state, α_{SE} is reduced by higher stall entry pitch rates (q_{SE} ≥ 5 deg/s). A comparison with the Brumby curve [13] shows that the $\Delta\alpha_S$ effects, for q_{SE}=0, fall within the envelope for mean $\Delta\alpha_S$ effects, whereas for $q_{SE}c/2U$=0.001 and 0.002, the Brumby mean $\Delta\alpha_S$ curve is exceeded by roughly 200%. Ground effect increased the lift curve slope, $\partial(\Delta C_{LGE})/\partial\alpha$, and varied with wing roughness state, where C_{LGE} is the lift coefficient in ground effect.

The flight test analysis will quantify the effects of pitch rate and surface roughness on dynamic stall onset. Through the analytical scheme shown in Fig. 2, the pitch-rate induced effects of viscous motion coupling with flow separation will be incorporated in a dynamically equivalent simulation of transport airplane stall at take off. The methodology is being extended to swept-wing airplanes through parallel tests and analysis of the NRC Falcon DA20.

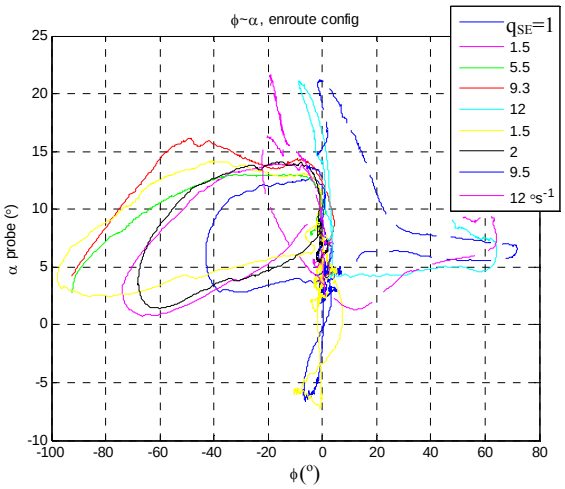

Figure 11: Angle of attack cross-plot with roll angle, showing bifurcated behavior between the lower rate stalls (q_{SE} < 5 deg/s) and higher rate stalls (#40 grit sandpaper, en-route configuration, 9 tests).

7 CFD Development and Analysis

The numerical approach is based on 2D and 3D URANS calculations for the CT-133, and a 3D URANS model for the Falcon. The FLOWer code [14] will be used for all of the flow simulations. This code was further developed, for this study, by implementing physical roughness modeling in the Wilcox k-ω [15] and Menter SST k-ω [16] turbulence models. The roughness parameter k_s/c appeared explicitly in these formulations. The extension and implementation of the turbulence models focused on the challenging requirement of accurately predicting both the boundary layer and free shear layer flows. A multi-block structured grid allows application of roughness in patches. The code will also be run in the unsteady mode to capture the dynamic pitch rate effects (see Section 3.2).

As described in Section 3.2, the CFD models will be used to predict the pressure distributions and flow separation characteristics during dynamic stalls in free flight at altitude ($h\rightarrow\infty$), and are then run in ground effect ($h\rightarrow 0$) to calculate the stall onset at take off (which cannot be achieved in flight).

For the purposes of CFD code validation, modeling of turbulent or mixed flows past fully or partially roughened cylinders (unsteady) and airfoils (steady and unsteady) was investigated to assess the roughness effect on the quasi-steady and transient flow behavior, and on the aerodynamic performance, including lift and drag forces. As expected for a bluff body, such as a cylinder, or airfoil with deployed flap, these flows were highly unsteady.

8 CFD Validation

The validation of the RANS/URANS simulations encompasses test cases involving natural flow unsteadiness (e.g. a fully rough circular cylinder), and motion-induced unsteadiness (rough/smooth airfoils and wings in oscillatory/ramping motions). For the flow past a cylinder [17], the validation was performed by comparing the CFD predicted results with the experimental data [18]-[19]. To illustrate the performance of the code in handling surface roughness and motion-induced unsteadiness the computed solutions are compared with experimental results for an airfoil with a rough leading edge, and for an oscillating wing, respectively.

Steady-state two-dimensional numerical flow solutions are presented for the NACA 65_1-212 airfoil with carborundum grit applied from the leading edge to the 8% chord position. The freestream flow conditions were given by a Mach number of M_∞=0.14, a Reynolds number based on the chord of $Re_c=6\times10^6$ and a relative roughness height of $k/c \approx k_s/c = 45.8\times10^{-5}$ (approx-

imating the "standard roughness" in Ref. [20]).

A multi-block structured grid topology was implemented, with about 350 points around the airfoil. In the normal direction, 160 grid points were used from the wall to the far field, which was located at 50 times the chord away from the model. The grid generation near the wall was performed to allow a small y^+ at the first grid point from the wall of about 1.4 near the suction peak at the maximum lift coefficient. The discretisation of Jameson-Schmidt-Turkel (JST) was used for the convective terms of the Navier-Stokes equations while a first-order Roe upwind scheme was implemented in the case of the convective terms of the turbulence equations. As described in Reference [14], the steady-state solutions were obtained using the explicit Runge-Kutta scheme for the Navier-Stokes equations and the DDADI-scheme for the turbulence equations.

Figure 12 displays the Mach number distribution around the airfoil at an angle of attack of 11 degrees. Since the leading edge region of the airfoil was rough, trailing edge stall occurred at lower angles of attack, reducing the maximum lift coefficient.

Figure 13 shows the airfoil lift coefficient variation with angle of attack. Good agreement was observed between the simulations and experimental data [20], for both of the turbulence models considered. As expected, both the maximum lift and the angle of attack for maximum lift were reduced drastically by the roughness effect. Comparing the predictions obtained using the two turbulence models, it appears that the Menter turbulence model predictions were slightly below the Wilcox ones. However, the results of both models agreed well with the experimental data. It should be noted that, while exact agreement was not expected because of the presence of 3D flow effects, the results should be acceptable at incipient stall conditions.

In the URANS time-accurate simulation involving airfoil oscillation, a fully implicit scheme was adopted. As

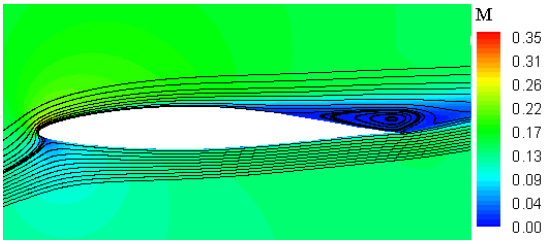

Figure 12: Mach number distribution around the NACA 65_1-212 airfoil with 8%c roughness near the leading edge. M_∞=0.14, Re_c=6×10^6, α=11 deg, roughness height k/c ≈ k_s/c = 45.8×10^{-5}.

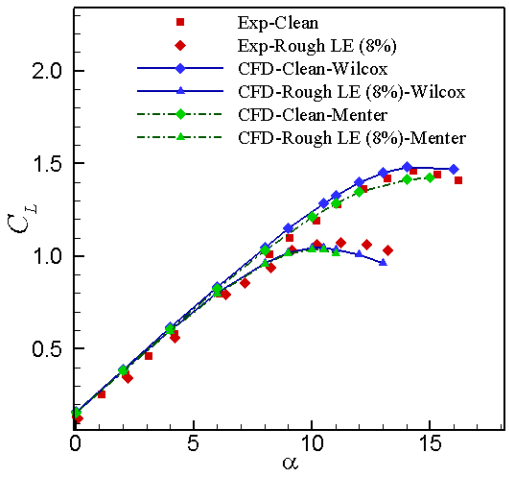

Figure 13: Lift coefficient versus angle of attack for the NACA 65_1-212 airfoil with clean and rough configurations. M_∞=0.14, Re_c=6×10^6, α=11 deg, roughness height k/c ≈ k_s/c = 45.8×10^{-5}.

implemented in the FLOWer code [14], a dual time-stepping method, which is characterized by pseudo-time iterations within each physical time step, was used. To compute unsteady flows past an airfoil, a steady-state solution was first computed at the mean angle of attack; then, after convergence, the time-accurate simulation with body motion is activated. The computations were second-order accurate in time and space, which required two previous, successive time levels to perform the computation for the new time level. The dimensionless time step was chosen to be 0.001-0.01, with inner iterations varying from 10 to 40 according to the prescribed convergence tolerance (5×10^{-5}) within each time level. The airfoil oscillation was characterized by $\alpha(t) = \alpha_0 + \Delta\alpha \sin(2\pi t / T)$, where t is the dimensionless time and T is the oscillation period. In the FLOWer code,

time was scaled according to $\tilde{t} = t\,(L/L_g)/\sqrt{RT_\infty}$, where L is the model characteristic length and L_g the grid unit, R is the gas constant, T_∞ is the free stream temperature, and $\tilde{t}$ is the dimensional time.

The 2D URANS simulation was validated for several airfoil pitching cases. Piziali's results [21] for the NACA 0015 oscillating in and out of stall are discussed here. At α_0=10.88°, $\Delta\alpha$=4.22°, $\boldsymbol{k}$=0.095, Re_c=1.953×10^6 and M_∞=0.291, the light stall generated the hysteresis loop shown in Fig. 14, where $\boldsymbol{k}$ is the reduced frequency. As a boundary layer trip at 0.005c was used on the aspect ratio 5 model, fully turbulent solutions could be compared with the experimental data in Fig. 14. Good convergence was obtained for time steps Δt=0.01, 0.0025 and 0.001, and grid convergence was demonstrated. The agreement with experiment (depicted for the span-wise station y/Y=0.5) was quite good, and although the lift was slightly higher, possibly due to 3D effects in the experiment, the general shape of the loop was faithfully replicated. Subtle differences between the computed and measured lift on the pitch downstroke could be attributed to effects of the boundary layer trip at stall, and on flow reattachment. This 2D solution was also in general agreement with 3D calculations made by Ekaterinaris [22] and Ekaterinaris and Platzer [23], using one-equation models. The measure of agreement obtained with the fully turbulent calculation was not unexpected as the effect of the laminar flow up to the trip is expected to be small at this Reynolds number and, in the presence of the trip, the moving wall effect is, for practical purposes, eliminated. Snapshots of stream-lines and Mach number distributions around the oscillating airfoil are shown in Fig. 15, which shows attached flow when the airfoil executes the pitching upstroke (Fig. 15a) and separated flow on the downstroke (Fig. 15b).

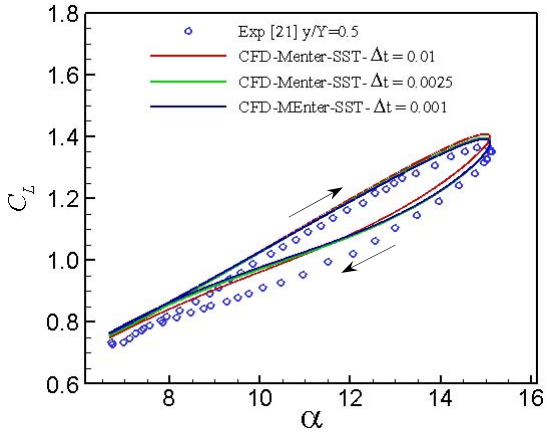

Figure 14 Computed aerodynamic lift for oscillating NACA 0015 airfoil with comparison to experimental data at M_∞=0.291, Re_c=1.953×10^6 and $\boldsymbol{k}$=0.095.

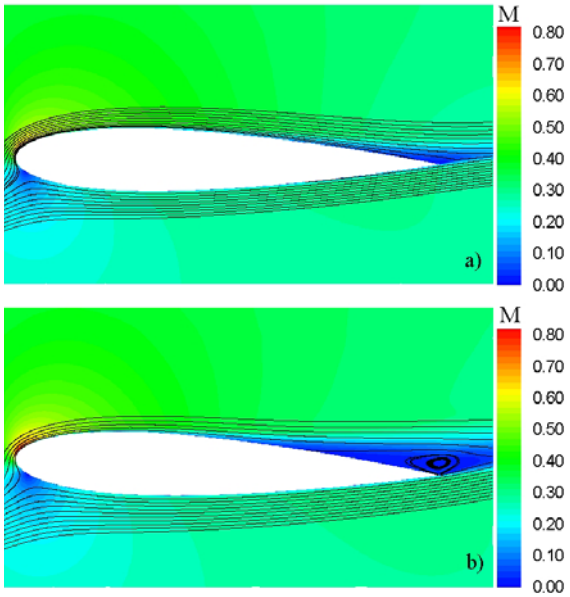

Figure 15 Mach number distribution past the NACA 0015 airfoil in oscillatory motion at M_∞=0.291, Re_c=1.953×10^6 and $\boldsymbol{k}$=0.095; a) α=11.77° (upstroke), and b) α=13.15° (downstroke).

9 Conclusions

The NRC program on dynamic stalling of transport airplanes has spawned a compre-hensive experimental/analytical approach which, in its first phase, has elucidated the factors determining stall onset on a straight wing airplane, and laid the groundwork for extension to swept wing airplanes in the second phase of the program. The following conclusions can be drawn.

The flight test results demonstrate that the effects of pitch rate, surface roughness

and ground proximity are nonlinearly coupled. The 3D roughness characterization and modeling introduced is applicable to arbitrary contamination types. The progression of unsteady flow separation on the airplane wing can be captured by in-flight infrared thermography. The URANS code with Wilcox k-ω and Menter SST k-ω turbulence models modified to handle surface roughness has been validated against experimental results for rough airfoils and for an oscillating wing.

Acknowledgement

The authors recognize the contributions of Marc Genest (SMPL/NRC), Matthew Bastian and Hub Stapper (FRL/NRC) to the flight test experiments. The authors would like to thank Dr. Jochen Raddatz and Dr. Thorsten Schwarz from DLR- Institut für Aerodynamik und Strömungstechnik for their support in running and developing the DLR-FLOWer code for roughness modeling.

References

[1] Brown AP and Beyers ME. Survey of jet transport incident/accidents with pitch-rate induced abrupt wing stalling near the ground, *AIAA*-2006-6270, 2006.

[2] Anon. Aircraft Accident report, Ryan international airlines DC-9-15, N565PC Loss of control on takeoff Cleveland-Hopkins International Airport, Cleveland, Ohio, February 17, 1991, *National Transportation Safety Board NTSB/AAR-91/09, PB91-910410*, Nov. 16, 1991.

[3] Beyers ME and Brown AP. Pitch-rate induced abrupt wing stalling of straight wing aircraft, *AIAA*-2006-6001, 2006.

[4] Brown AP, Beyers ME and Bastian M. Dynamic stall flight data, effects of pitch rate, surface roughness and ground effect, *AIAA*-2008-0201, 2008.

[5] Ericsson LE and Reding JP. Fluid dynamics of unsteady separated flow, Part II. Lifting surfaces, *Prog. Aerospace Sci*., Vol. 24, pp.249-356, 1987.

[6] Ericsson LE and Beyers ME. Universality of the moving wall effect, *Journal of Aircraft*, Vol. 37, No.2, pp 508-513, 2000.

[7] Dumitrescu H and Cardos V. Moving-wall effect on unsteady boundary layers, *Journal of Aircraft*, Vol. 37, No. 2, pp 341-345, 2000.

[8] Ericsson LE and Reding JP. Dynamic overshoot of the static stall angle, *Journal of Aircraft*, Vol. 22, 7, p. 637, 1985.

[9] Beyers ME and Ericsson LE. Phenomenology of airplane dynamic stall, in preparation, 2008.

[10] Nikuradse J. Untersuchungen über die Geschwindigkeitsverteilung in turbulenten Strömungen, Forsch.-Arb. Ing.-Wes. Heft 281, Berlin, 1926.

[11] Schlichting H. Experimental investigation of the problem of surface roughness, NACA TM No. 832, 1936.

[12] Jiménez J. Turbulent flow over rough walls, *Ann. Rev. Fluid Mech*. Vol. 36, pp. 173-196, 2004.

[13] Brumby RE. The effect of wing ice contamination on essential flight characteristics, *Douglas Aircraft Company*, 68th AGARD Fluid Dynamics Panel Specialists Meeting, April 29-May 1, 1991.

[14] Anon. FLOWer Installation and user handbook, Institute of Aerodynamics and Flow Technology of the German Aerospace Center (DLR), Doc. Nr. MEGAFLOW-1001

[15] Wilcox DC. *Turbulence modeling for CFD*, DCW Industries Inc., Second Edition, 1998.

[16] Hellsten A and Laine S. Extension of the k-ω-SST turbulence model for flows over rough surfaces, *AIAA*-97-3577, pp. 252–260, 1997.

[17] Mamou M, Beyers M, Dagdougui H and Hasnaoui M. Modeling of unsteady turbulent flows past roughened circular cylinders and airfoils, *BBAA VI International Colloquium on Bluff Bodies Aerodynamics & Applications*, Milano, Italy, July 2008.

[18] Achenbach E. Influence of surface roughness on the cross-flow around a circular cylinder, *Journal of Fluid Mechanics*, Vol. 46, pp. 321–335, 1971.

[19] Nakamura NY and Tomonari Y. The Effects of surface roughness on the flow past circular cylinder at high Reynolds numbers, *Journal of Fluid Mechanics*, Vol. 123, pp. 363–378, 1982.

[20] Abbott H, von Doenhoff AE and Stivers LS. Summary of airfoil data, NACA Report No. 824, 1945.

[21] Piziali RA. 2-D and 3-D oscillating wing aerodynamics for a range of angles of attack including stall, *NASA-TM-4632*, 1994.

[22] Ekaterinaris JA. Numerical investigation of dynamic stall of an oscillating wing, *AIAA Journal*, Vol. 33, No. 10, Oct. 1995.

[23] Ekaterinaris JA and Platzer MF. Computational prediction of airfoil dynamic stall, *Prog. Aerospace Sci.*, Vol. 33, pp. 759-846, 1997.

Copyright Statement